International Journal of Nanomedicine

Dovepress
Taylor & Francis Group

Open Access Full Text Article

ORIGINAL RESEARCH

Development of Cytolytic Iridium-Complexed Octaarginine Peptide Albumin Nanomedicine for Hepatocellular Carcinoma Treatment

Xingwei Sun[1,*], Di Wang[1,*], Shiwei Chang[2,*], Liang Yin[1], Hao Zhang[1], Shuangshuang Ji[2], Hao Fei[2], Yong Jin[1]

[1]Department of Interventional Radiology, The Second Affiliated Hospital of Soochow University, Suzhou, 215004, People's Republic of China; [2]Nanobiomedicine Division, Suzhou Institute of Nano-Tech and Nano-Bionics, Chinese Academy of Sciences, Suzhou, 215123, People's Republic of China

*These authors contributed equally to this work

Correspondence: Yong Jin, Email jinyong@suda.edu.cn, Hao Fei, Email hfei2008@sinano.ac.cn

Objective: Hepatocellular carcinoma is one of the most challenging malignancies and has high incidence and mortality rates worldwide. Digital subtraction angiography (DSA)-guided hepatic arterial infusion of the standard chemotherapeutic agent oxaliplatin (OXA) has the advantages of both precision and efficacy, making it an important therapeutic strategy for advanced-stage liver cancer. However, patients receiving this treatment still face severe systemic toxicity and poor tolerability of oxaliplatin.

Methods: In this study, we compared oxaliplatin with novel albumin-formulated oncolytic peptide nanoparticles, Ir-cR8 (abbreviated as iPep), in the treatment of orthotopic liver cancer in a mouse model by intravenous injection and in a rabbit model via DSA-guided hepatic arterial infusion.

Results: The results showed that intravenous Ir-cR8-BSA-NPs had enhanced inhibitory effects to the growth of H22 ectopic liver tumors in mice and also with reduced toxicity in animals compared to OXA treatment. Specifically, Ir-cR8-BSA-NPs-treated mice showed approximately 92% tumor growth inhibition compared to approximately 88% for OXA. In the rabbit VX2 ectopic hepatocellular carcinoma model, Ir-cR8-BSA-NPs demonstrated significantly stronger inhibition ($P<0.01$) of tumor size compared to OXA, as assessed by PET/CT imaging, with SUV values decreasing from 5.15±0.46 to 2.52±0.57, compared to OXA-treated group, which decreased from 5.44±0.43 to 3.90±0.24. Furthermore, Ir-cR8- BSA-NPs significantly improved stability by albumin encapsulation and reduced hemolytic toxicity ($P<0.001$), resulting in improved therapeutic efficacy.

Conclusion: This study demonstrated the combined advantages of a novel membrane-active oncolytic peptide nanomedicine and precise drug delivery enabled by arterial infusion technology for the interventional treatment of liver cancer.

Keywords: interventional treatment, hepatocellular carcinoma, Ir-cR8-BSA-NP, microspheres, nanomedicine

Introduction

Hepatocellular carcinoma (HCC) is one of the most common malignancies in clinical practice. According to statistics from 2023, there were approximately 900,000 new cases and 830,000 hCC-related deaths worldwide, making HCC the third leading cause of cancer-related deaths worldwide.[1–6] Common methods for curing HCC include liver resection, liver transplantation and ablation therapy; however, only 20–30% of patients are eligible for curative surgery. Owing to the insidious onset of liver cancer in most patients, HCC is often diagnosed at an advanced stage, resulting in poor prognostic outcomes.[7,8] Hepatic artery infusion chemotherapy (HAIC) is an important treatment modality for advanced-stage liver cancer. However, the severe systemic toxicity of the first-line chemotherapeutic agent oxaliplatin has led to poor tolerability in patients at this stage, resulting in forced discontinuation of treatment.[9,10] Therefore, there is an urgent need to develop alternative drugs that are safe and effective and have low toxicity, especially for patients with advanced liver cancer.

Received: 11 November 2024
Accepted: 21 January 2025
Published: 25 February 2025

Unlike traditional chemotherapeutics that target DNA, microtubules or telomerases, a class of peptide-based "weapons" that target biological membranes in cells has been widely found in nature and is under medical development. We have recently reported several cationic amphipathic designer peptides as potential drugs with novel anticancer mechanisms. In particular, iridium-complexed oligoarginine peptides are formed by the coordination of 2-phenylpyridine complexed with iridium(III) and histidine residues. The octaarginine peptide, a classic cell-penetrating peptide with low toxicity, is a component of the anticancer compound Ir-cR8[11–13] that is created by introducing hydrophobic moieties through iridium (III) coordination, increasing the toxicity of octaarginine while imparting optical activity to the molecule;[14,15] its distinct amphipathic structure is characterized by a compact hydrophobic $Ir(ppy)_2$ group and a rigid cyclic cationic domain (Figure 1A). Research has shown that iridium-complexed octa-arginine peptides have promising antitumor effects. However, the hemolytic toxicity of Ir-cR8 is significant, and Ir-cR8 lacks stability in serum.[16,17]

Serum albumin, with a concentration of about 40 mg/mL in human blood and a molecular weight of 66.5 kDa, is non-toxic, biocompatible, biodegradable and non-immunogenic.[18–20] To address the hematotoxicity and instability of Ir-cR8, in this study, bovine serum albumin was used to assemble Ir-cR8 into albumin-prepared nanoparticles (Ir-cR8-BSA-NPs), which significantly improved the stability of the peptide and reduced the hemolytic toxicity. This serum albumin-based pre-coated active octa-arginine peptide (iPep) has been reported in our previous work and has shown potential in cancer chemotherapy and

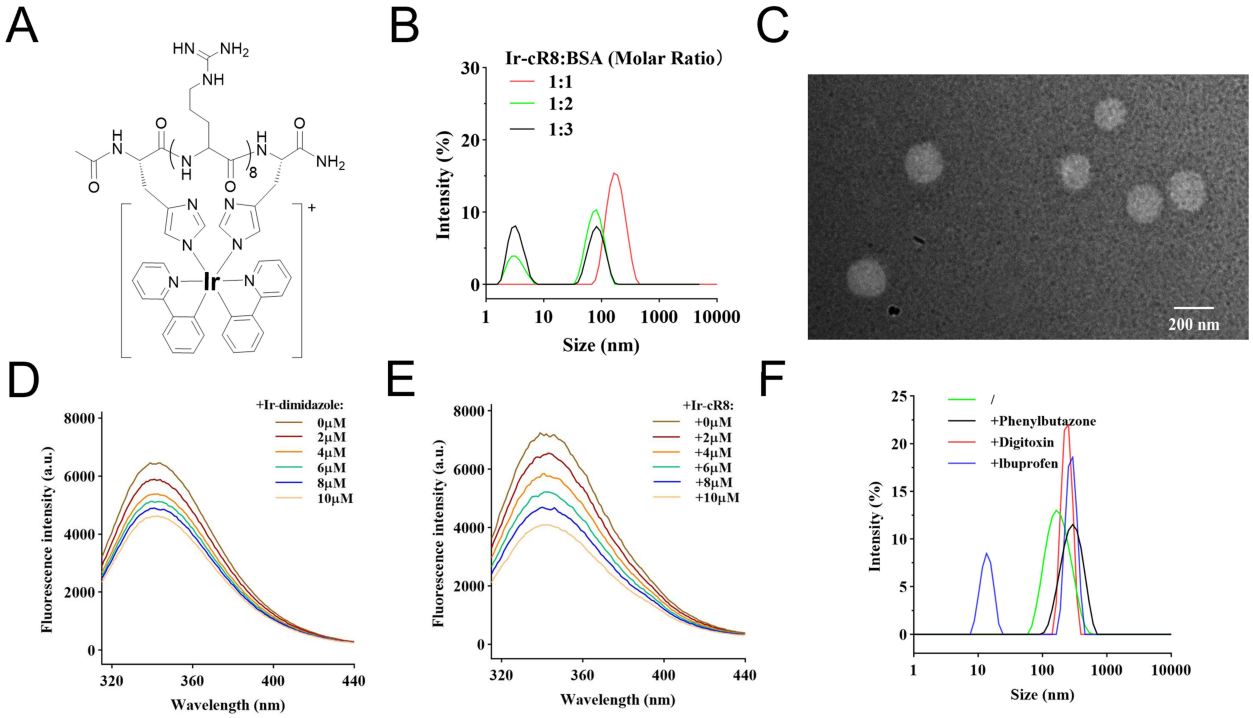

G

Site marker	K_b ($10^6 M^{-1}$)	n	R^2
/	0.52	1.172	0.9962
Phenylbutazone	0.68	1.198	0.9998
Ibuprofen	0.24	1.099	0.9952
Digitoxin	0.73	1.204	0.9985

H

	H22	VX2	BMDC	BMDM
Ir-cR8	6.20±0.19	12.38±1.18	9.8±0.2[a]	14.2±2.0[a]
Ir-cR8-BSA-NP	9.95±0.28	16.57±1.52	35.16±7.09	40.22±11.37
OXA	21.52±0.88	24.41±2.07	7.6±1.1[a]	4.6±0.1[a]

Figure 1 (**A**) Chemical structure of Ir-cR8. (**B**) Particle size distributions of Ir-cR8 and BSA mixtures at ratios of 1:1, 1:2 and 1:3. (**C**) Transmission electron microscopy (TEM) images of Ir-cR8-BSA-NPs; scale bar, 200 nm. (**D**) Fluorescence quenching spectra of BSA by Ir-diimidazole. (**E**) Fluorescence quenching spectra of BSA by Ir-cR8. (**F**) Particle size distribution of the mixture of Ir-cR8 and BSA in the presence and absence of site-competitive compounds. (**G**) Binding constants (Kb) and binding sites (n) of Ir-cR8 for BSA. (**H**) Measured half-maximal inhibitory concentrations (IC50s) of Ir-cR8, NP and oxaliplatin against cancer cells and immune cells. The numerical units are in the micron scale. [a]The data in the table are derived from Ref.[13]

immunotherapy.[13] This nanoparticle (NP) effectively triggered stress-mediated 4T1 cell necrosis through intrinsically amphiphilic-driven bimodal interactions, thereby inducing potent immune activation beyond a wide range of known immunogenic drugs. In this study, we will explore the potential of Ir-cR8 as a novel anticancer compound and investigate its application in the treatment of hepatocellular carcinoma. We will explore whether Ir-cR8 is effective in inhibiting the growth of hepatocellular carcinoma and whether it is safer and more effective than existing standard chemotherapeutic agents in the following aspects. This includes comparing the effectiveness of Ir-cR8 with the standard chemotherapy drug oxaliplatin in inhibiting the growth of hepatocellular carcinoma. And evaluate the stability and hemolytic toxicity of Ir-cR8 and how these properties affect its in vivo efficacy. And explore the potential of Ir-cR8 to improve drug stability and reduce toxicity after binding to albumin to form nanoparticles (Ir-cR8-BSA-NPs). We expect that this study will provide a safer and more effective therapeutic option for patients with hepatocellular carcinoma and provide new insights into the study of peptide anticancer drugs.

Experimental

Animal Ethics Statement

The experiment was approved by the Ethics Committee of Soochow University and all experiments were conducted in accordance with relevant institutional and national guidelines and regulations.

Preparation and Characterization of the NPs

The hydrodynamic particle size and polydispersity index (PDI) of the NPs were determined by dynamic light scattering (DLS) technique, which showed that the particle size was 170.87 ± 7.69 nm, and the PDI was less than 0.2, indicating that the NPs had a uniform particle size distribution. Transmission electron microscopy (TEM) images further confirmed the spherical morphology and consistent size of the NPs. To assess the purity of the NPs, we used high-performance liquid chromatography (HPLC) analysis, which showed that the purity of Ir-cR8-BSA-NPs was higher than 95%. In addition, we performed stability tests on the NPs, including changes in particle size and PDI after storage at 4°C and room temperature for different periods of time, and the results showed that the NPs remained stable for at least 6 months. All NPs batches passed endotoxin and sterility tests to ensure their biosafety. To ensure batch-to-batch consistency, three consecutive batches of NPs were analyzed by DLS and HPLC, and the results showed that the batch-to-batch variation was within acceptable limits.

Binding Mechanism

To investigate the binding properties, Ir-diim/cR8 and BSA were first mixed at molar ratios of 1:1, 1:2, and 1:3 for 2 h at room temperature and analyzed by DLS. Then, Ir-diim was added to the BSA solution (2 μM) at concentrations of 0, 2, 4, 6, 8, and 10 μM, and cR8 was added at concentrations of 0, 2, 4, 6, 8, 10, and 20 μM. To study the binding site of iPep in BSA, 1000 μM stock solution was diluted to 2 μM 1000 μL in each EP tube, and simultaneously, phenylbutazone/ibuprofen/digitoxin (final concentration of 2 μM) was added to each EP tube. Finally, Ir-cR8 was added to each EP tube so that the concentration of Ir-cR8 in each EP tube was 0, 2, 4, 6, 8, or 10 μM. The bimolecular burst rate constants, Kq, binding constants, Kb, and binding sites, n, were calculated according to the following formulas:

$$F_0/F = 1 + K_q \tau_0 [Q]$$

$$\log \frac{F0 - F}{F} = \log K_b + n \log Q$$

Fo and F are the steady-state fluorescence intensities of BSA in the absence and presence of the bursting agent, respectively, K_b is the binding constant, K_q is the bimolecular burst rate constant, Q is the concentration of the bursting agent, n is the number of binding sites, and is the average lifetime of a biomolecule, which is typically 10^{-8} s.[21] To further confirm the binding sites, BSA (10 μM) was mixed with phenylbutazone/ibuprofen/digitoxin (30 μM), and then 10 μM iPep was added to each group. The samples that contained only BSA (10 μM) or BSA+iPep (10 μM) were used as the control group. After rotary mixing at 25 °C for 2 h, 2 mL of each sample was removed, and the particle size distribution of each sample was examined by DLS. To explore the effects of charge and ratio on the assembly, Ir-cR4/Ir-

cR6/iPep and BSA were mixed at different molar ratios (Ir-cR4/Ir-cR6/iPep: HSA ratios of 2:1, 1:1, 1:2 and 1:3) with final concentrations of 10 μM in the tube and detected by DLS.

Cell Lines

The H22 murine hepatocellular carcinoma cell line was purchased from FuHeng Biology. The VX2 rabbit squamous cell carcinoma cell line was purchased from Shanghai Guandao Biological Engineering Co. BMDC and BMDM were generated by dissecting the femurs of BALB/c mice (6–8 weeks) and rinsing the bone marrow cells into a 6-well cell culture plate using a syringe filled with 1× PBS (pH 7.4). The cells were subsequently lysed with erythrocyte lysis buffer for 2 minutes and washed 3 times, after which half of the cells were incubated for 3 days with RPMI 1640 medium containing 10% FBS and 20 ng/mL GM-CSF and IL-4. The medium was then replaced with fresh medium containing the same cytokines, and the mixture was incubated for another 4 days to collect nonadherent cells. To induce BMDMs, 20 ng/mL M-CSF was added, and adherent cells were collected.

Cell Death Morphology Observation

H22 cells in the logarithmic growth phase were centrifuged and resuspended in complete RPMI 1640 medium (RPMI 1640 + 10% FBS + 1% double antibody). The density of H22 cells was adjusted to 2×10^5 mL-1. One hundred microliters of H22 cell suspension was uniformly added to each well of a 96-well glass-bottomed plate so that the number of cells in each well was 2×10^4. Ir-cR8-BSA-NPs (15 μM) and propidium iodide (PI, 10 μg-mL^{-1}) were added after the supernatant was discarded. Finally, confocal microscopy was used to observe the interaction of the nanoparticles with H22 cells in real time, with one image collected every 5 s. The nanoparticles were observed in real time by confocal microscopy.

Selective Cytotoxicity Assays

Detection of the Toxicity of Ir-cR8, Ir-cR8-BSA-NPs and Oxaliplatin to H22 Cells Using a CCK-8 Assay

H22 cells in the logarithmic growth phase were digested, centrifuged and resuspended in RPMI 1640 basal medium. After cell counting, the density of H22 cells was adjusted to 4×10^5 mL-1. Fifty microliters of H22 cell suspension was added uniformly to each well of a 96-well cell culture plate so that the number of cells in each well was 2×10^4. Fifty microliters of Ir-cR8/Ir-cR8-BSA-NPs/oxaliplatin was added sequentially in accordance with the concentration gradient (at this time, the final concentration of each drug was 1/2 of the original concentration), and at the same time, RPMI 1640 basal medium was added as a control, and blank wells were set up. Three parallel groups were set up for each concentration of the above drugs. Finally, 100 μL of PBS buffer was added to each well of the outer layer of the 96-well cell plate and incubated at 37 °C with 5% carbon dioxide for 24 h. After 24 h, 10 μL of CCK-8 assay solution was added to each well, and the plate was incubated in the incubator for 2 h. Finally, the absorbance at 450 nm was read by an enzyme marker to calculate the half-maximal inhibitory concentration (IC50) value.

Detection of the Toxicity of Ir-cR8, Ir-cR8-BSA-NPs and Oxaliplatin to VX2 Cells Using a Thiazolyl Blue (MTT) Assay

VX2 cells in the logarithmic growth phase were digested, centrifuged, and resuspended in RPMI 1640 complete medium. After cell counting, the density of VX2 cells was adjusted to 8×10^4 mL^{-1}. One hundred microliters of VX2 cell suspension was added uniformly to each well of a 96-well cell culture plate so that the number of cells in each well was 8×10^3. One hundred microliters of PBS buffer was added to each well of the outer layer of the 96-well plate, and the plate was incubated at 37 °C with 5% carbon dioxide for 24 h. The culture medium was removed from the 96-well plate and discarded, after which 100 μL of Ir-cR8/Ir-cR8-BSA-NPs/oxaliplatin was added in accordance with the concentration gradient, RPMI 1640 basal medium was added as the control group, and blank wells were set up. Three parallel groups were set up for each concentration of drugs above. After incubation for 24 h, the drug culture mixture was discarded from the 96-well plate, 120 μL of RPMI 1640 basal medium containing MTT (0.83 mg.mL^{-1}) was added to each well, and the incubation was continued for 4 h. MTT was discarded from the 96-well plate, 150 μL of DMSO was added, and the mixture was shaken to fully dissolve the formazan in the wells. Finally, the absorbance at 490 nm was read using an enzyme counter to calculate the IC50 value of the half-inhibitory concentration (IC50).

Mouse in Situ Hepatocellular Carcinoma Model

An orthotopic mouse model of hepatocellular carcinoma in 6- to 8-week-old female BALB/c mice was established using mice obtained from Suzhou Jingweiyu Biotechnology Co., Ltd. H22 cells in the logarithmic growth phase were digested, centrifuged and adjusted to a density of 2×10^6 cells/mL. Each mouse was inoculated with 10^6 cells mixed with standard matrix gel. Surgical procedures included an anterior abdominal incision, surgical forceps clip out liver lobe, injection of cells and closure of the incision. When the tumor size reached approximately 50 mm^3, the mice were divided into three groups (n=5): the control group received an i.v. injection of 100 μL of PBS; the Ir-cR8-BSA-NP group received an i.v. injection of 100 μL of Ir-cR8-BSA-NPs (500 mm) for 6 consecutive days; and the oxaliplatin group received an i.v. injection of oxaliplatin (5 mg/kg) every two days for a total of three injections. Starting on the day of tumor inoculation, on Days 5, 10 and 15, each mouse received an intraperitoneal injection of 200 μL of 15 mg/mL D-luciferin sodium salt. Tumor growth was monitored using an IVIS Spectrum system (IVIS Lumina XRMS Series III, PerkinElmer), and the weight of each mouse was recorded.

Tissue Distribution Assay

iPeps and NPs were diluted with DMEM to 0.1, 0.5, 1 and 2 μM, respectively. The fluorescence emission intensity at 520 nm was detected using a fluorescence spectrophotometer with an excitation wavelength of 328 nm, an Em slit of 10.0 nm, and 700 V. H22-loaded tumor-bearing mice were injected with 50 mmol of iPep or NP into the tail vein. Twenty-four hours later, the mice in each group were sacrificed, and heart, liver, spleen, lung, kidney and tumor tissues were collected separately. After being weighed, the tissues were cut into approximately 2 mm^3 pieces, digested with RIPA buffer (high) at a ratio of 150 μL/20 mg, and then pulverized using an ultrasonic homogenizer. One milliliter of homogenate was taken and centrifuged at 12,000 × g for 10 min, and 500 μL of the supernatant was taken to detect the fluorescence emission intensity at 520 nm. The drug concentration was calculated based on the standard curve established above.

Histological Staining

Three days after injection, tissues (heart, liver, spleen, lung, kidney and tumor) were collected and fixed in 4% neutral paraformaldehyde. After 24 hours of fixation, the samples were paraffin-embedded, and the sections were stained with hematoxylin and eosin (HE). The stained tissue sections were observed under a fluorescence upright microscope (Axio Scope A1, Zeiss).

Rabbit VX2 Orthotopic Liver Tumor Experiments

To further validate the efficacy of Ir-cR8-BSA-NPs and oxaliplatin, a rabbit VX2 orthotopic liver cancer model was generated from 4-month-old New Zealand White rabbits (n=4 per group). The rabbits were divided into three groups: control (PBS, arterial infusion of PBS), oxaliplatin (arterial infusion of oxaliplatin 5 $mg\text{-}kg^{-1}$) and Ir-cR8-BSA-NP (arterial infusion of Ir-cR8-BSA-NP 5 $mg\text{-}kg^{-1}$) groups. The dose of Ir-cR8-BSA-NPs and oxaliplatin arterial perfusion treatment was calculated according to the body surface area-converted dose formula $Dose(b)=Dose(a)\times(kb/ka)\times(Wb/Wa)^{2/3}$. Where Dose(a) is the dose for known animal a (mg/animal) and Dose(b) is the dose for desired animal b (mg/animal); ka and kb are body size coefficients see Table S1; Wa and Wb are body weights (kg).

Under ultrasound guidance (Supplementary Figure 1), 1 mm^3 blocks of tumor tissue were injected into the left lobe of each rabbit liver using a 20-gauge needle. Postoperatively, the rabbits received intramuscular injections of 40 WU/d penicillin sodium for 3 consecutive days to prevent infection. Tumor size was measured by computed tomography (CT) after surgery.

The doses used for arterial infusion treatment with Ir-cR8-BSA-NPs and oxaliplatin were calculated based on body surface area using the formula Dose(b) = Dose(a) × (kb/ka) × (Wb/Wa)^(2/3). In situ VX2 tumors were treated by arterial infusion under digital subtraction angiography (DSA) guidance. The rabbits in each group underwent PET/CT before treatment and 7 days after infusion. The standardized uptake values (SUVs) of the tumors for each group were compared before and after treatment to assess the antitumor effects.

At the end of the experiment, the rabbit livers were harvested, the tumor tissues were isolated, and the tissues were immersed in 4% neutral paraformaldehyde. After 24 hours of fixation, paraffin embedding was performed, and the

sections were stained with HE to further compare the necrotic conditions of the tumors in each group. These HE-stained images were obtained using a fluorescence upright microscope (Axio Scope A1, Zeiss).

Statistical Analysis

All the numerical data are expressed as the means ± s.d.s unless otherwise noted. The significance of differences between two groups was calculated using two-tailed Student's t tests. Statistical analysis was performed using OriginPro 2019b. Differences were statistically significant at *P < 0.05, **P < 0.01, ***P < 0.001 and ****P < 0.0001.

Results and Discussion

Bimodal Attractions Promote iPep and BSA Nanoassembly

Using dynamic laser scanning analysis (DLSA) and transmission electron microscopy, we observed spontaneous formation of nanoparticles at a ratio of 1:1 M in physiological buffer conditions (Figure 1B and C). The structure of iPep was then subdivided into an oligomeric nine-peptide structural domain (cR8) and a hydrophobic structural domain ($Ir(ppy)_2$-diimi dazole or hereafter Ir-diim) to further explore the contribution of each structural domain to the assembly. The DLSA results revealed that more efficient assembly occurred when the molar ratio of Ir-cR8:BSA was 1:1 (Figure 1B). We hypothesize that the peptide and $Ir(ppy)_2$ structural domains synergistically promote assembly through a more defined mechanism than nonspecific adsorption. The presence of tryptophan (Trp) in the hydrophobic cavity of bovine serum albumin substructural domain IIA is critical for the intrinsic fluorescence of albumin. Tryptophan (Trp-214) fluorescence emission is often used to probe how hydrophobic compound binding perturbs the internal environment of serum albumin.[22] We found that Ir-diim (2–10 μM, Figure 1D) could quench Trp-214 emission, and Ir-cR8 could quench even more (Figure 1E), suggesting that the insertion of the $Ir(ppy)_2$ motif into the hydrophobic pocket of bovine serum albumin and the structural domains of the cationic polypeptide enhanced the interaction. Using this set of quench rate curves, we calculated the bimolecular quenching rate constant (Kq) to be 7.99×10^{12} $L\cdot mol^{-1}\cdot s^{-1}$ according to the Stern–Volmer equation, which was significantly greater than the maximum dynamic quenching rate constant of 2×10^{10} $L\cdot mol^{-1}\cdot s^{-1}$, according to which we were able to determine that the quenching process occurring between Ir-cR8 and albumin was static quenching; moreover, the two were not simply colliding but combining to form a nonluminous complex. The binding constant (Kb) of Ir-cR8 to albumin was calculated to be 0.52×10^6 M^{-1}, and the number of binding sites n was 1.17, R^2=0.9962. The crystal structure data revealed that albumin has three homologous α-helical domains, ie, structural domains I, II, and III, and that the hydrophobic cavities of substructural domains IIA and IIIA are the main binding sites of albumin and the drug-binding site. The hydrophobic cavity of substructural domains IIA and IIIA is the main binding site for albumin-ligand binding, drug-binding sites 1 and 2 are located in substructural domains IIA and IIIA, respectively, and drug-binding site 3 is located in the hydrophilic cavity of substructural domain IB.[23,24] Phenylbutazone Serum albumin, which is present in human blood at a concentration of approximately 40 mg/mL and has a molecular weight of 66.5 kDa, is nontoxic, biocompatible, biodegradable and nonimmunogenic binds specifically to serum albumin drug-binding site 1, whereas ibuprofen binds specifically to site 2, and digitalis toxin binds specifically to site 3. The binding sites of Ir-cR8 on BSA could be detected by a simple spectroscopic method in which phenylbutazone, ibuprofen and digitoxin were used as competing compounds for sites 1, 2 and.[25–27] The results revealed that the binding constants of Ir-cR8 to BSA with the addition of the competing compounds were 0.68×10^6 M^{-1}, 0.24×10^6 M^{-1}, and 0.73×10^6 M^{-1}, respectively (Figure 1G). Compared with the binding constant of Ir-cR8 to BSA of 0.52×10^6 M^{-1} without the addition of the competing compounds, the addition of the competing compound ibuprofen decreased the binding constants of Ir-cR8 and albumin, whereas the other two competing compounds had no inhibitory effect or even acted as promoters; thus, site 2 might be the binding site of Ir-cR8 on BSA. To further confirm that site 2 is the binding site of Ir-cR8 and BSA, a change in the particle size distribution of Ir-cR8 and albumin mixtures without/with site-competing compounds was observed. The results, as shown in Figure 1F, indicate that a mixture of Ir-cR8 and albumin at a molar ratio of 1:1 can form nanoparticles with an average hydrated particle size of 170 nm when no competing compounds are added. When albumin was mixed well with site-competing compounds (phenylbutazone/ibuprofen/digitoxin) and then Ir-cR8 was added, the group with the addition of ibuprofen produced a small peak at 10 nm, whereas the size of the particles in the group with the addition of the other two competing compounds did not change significantly, suggesting that ibuprofen affects the assembly of Ir-cR8 and albumin to some extent and demonstrating again that the binding of Ir-cR8 and albumin occurs at drug-binding site 2.

When Ir-cR8 and albumin were mixed at a molar ratio of 1:1, the average particle size distribution was 170.87 ± 7.69 nm. If Ir-cR8 and bovine serum albumin were only two-molecule conjugates formed through hydrophobic interactions, a particle size of 170 nm could not be reached; therefore, it was speculated that the cationic portion of Ir-cR8 might have electrostatic interactions with negatively charged BSA to promote the formation of a stable nanostructure. We examined the particle size distribution of peptides with different charges when mixed with bovine serum albumin at different molar ratios, and the results are shown in Supplementary Figure 2. Ir-cR4 has a low number of cations, and only a peak at approximately 100 nm appeared when it was mixed 2:1 with albumin. When mixed with albumin at a molar ratio of 1:1, Ir-cR6 and Ir-cR8 had average particle sizes of 224 nm and 170 nm, respectively. When the nanoparticle particle size was between 50 nm and 200 nm, it was favorable for the nanoparticles to accumulate at the tumor site. Thus, it is more appropriate to choose Ir-cR8 and albumin assembly for subsequent studies. In addition, the binding site n obtained from the above calculation was also approximately 1; therefore, the molar ratio of 1:1 is a more appropriate assembly ratio of Ir-cR8 and albumin. For the prepared formulations, we used an optimized 1:1 ratio of Ir-cR8-BSA nanoparticles (abbreviated as Ir-cR8-BSA-NPs) for the following studies.

Cellular-Level Studies of Ir-cR8-BSA-NPs

Toxicity Assay of Ir-cR8-BSA-NPs on H22 and VX2 Cells

The assembly of Ir-cR8 with BSA produced a stable nanostructure, and the addition of BSA made the peptide more stable and less susceptible to decomposition; however, whether the addition of BSA affects the toxicity of Ir-cR8 to tumor cells remains to be explored.[28–31] Oxaliplatin is a commonly used chemotherapeutic drug in the clinical treatment of hepatocellular carcinoma, and the anticancer potential of these nanoparticles was initially evaluated by comparison with that of oxaliplatin. Both H22 and VX2 cells are cancer cells; H22 cells are derived from mice, and VX2 cells are derived from rabbits. The results of the toxicity experiments are shown in Figures 1H and 2A–F. The half-maximal inhibitory concentrations (IC50s) of Ir-cR8 on H22 and VX2 were 6.20±0.19 μM and 12.38±1.18 μM, the half-maximal inhibitory concentrations (IC50s) of the nanoparticles on H22 and VX2 were 9.95±0.28 μM and 16.57±1.52 μM, and the peptide and albumin assembly killing activities did not decrease significantly. The half-maximal inhibitory concentrations (IC50s) of oxaliplatin on H22 and VX2 cells were 21.52±0.88 μM and 24.41±2.07 μM, respectively, and the half-maximal inhibitory concentrations were greater than those of the nanoparticle group. At the cellular level, the killing activity of the nanoparticle group was not inferior to that of the marketed drug oxaliplatin.

To assess the effects of Ir-cR8-BSA-NPs and other treatments on the liver, we monitored liver function indices in the serum of mice. As shown in Table S2, serum ALT, AST, TP, ALB, TBIL, and ALP levels in the Ir-cR8-BSA-NPs-treated group showed smaller changes compared with those in the healthy control group, suggesting that this treatment modality is less toxic to the liver. In particular, the ALT and AST levels in the Ir-cR8-BSA-NPs group (49.32 U/L and 148.73 U/L, respectively) showed a non-significant difference compared with those in the healthy control group (46.31 U/L and 150.08 U/L, respectively), suggesting that Ir-cR8-BSA-NPs inhibits tumor growth while having fewer side effects on the liver.

Selective Killing of Ir-cR8-BSA-NPs

Cationic membrane-active peptides generally carry a certain positive charge. Tumor cell membranes carry more negative charges than normal cells do; therefore, the difference in electrostatic interactions between peptides and the two cell membranes may lead to a certain degree of selective killing ability.[32,33] Although some chemotherapeutic drugs have been shown to cause immunogenic death of tumor cells, due to their mechanisms of action, the killing of tumor cells is accompanied by toxicity to immune cells, which hampers the immune function of the body. We examined the toxicity of NPs on H22, BMDC, and BMDM cells. The results (Table 1) revealed that the toxicities of the NPs to BMDCs and BMDMs were significantly weaker than that to H22 cells, indicating that the NPs had some degree of killing selectivity. The potentials of the three cell types were subsequently measured, and the results, as shown in Supplementary Figure 3, revealed that the electronegativity of the surface of H22 cells was significantly greater than those of the two immune cell types and that the NPs had a net positive charge; thus, the NPs were more inclined to electrostatically interact with H22 cells, which could be the reason for the difference in killing.

https://doi.org/10.2147/IJN.S502257

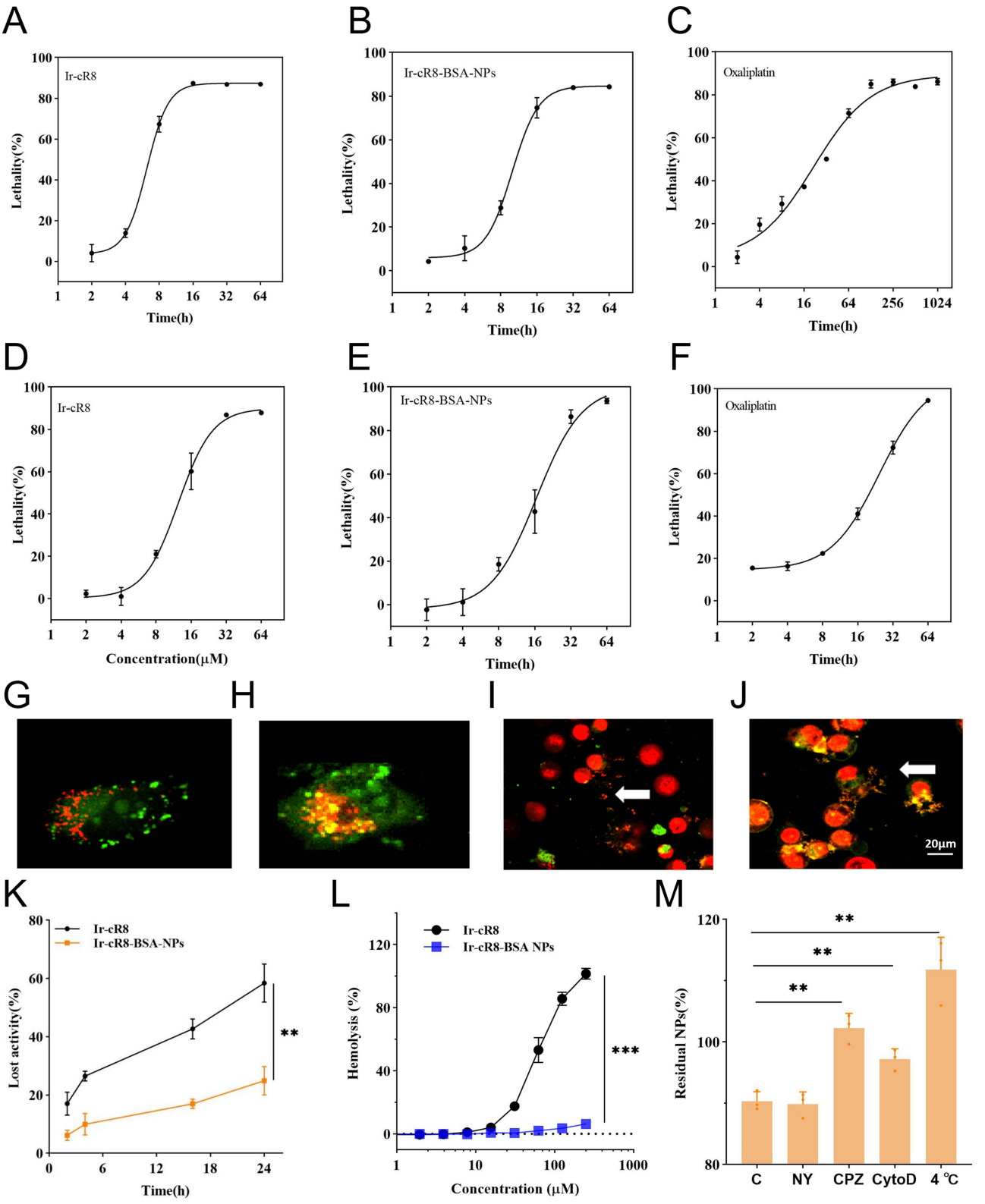

Figure 2 (**A–C**) Toxicity assays of Ir-cR8, oxaliplatin and Ir-cR8-BSA-NPs in H22 cells. (**D–F**) Toxicity assays of Ir-cR8, oxaliplatin and Ir-cR8-BSA-NPs in VX2 cells. (**G–H**) Colocalization of Ir-cR8 (left) and Ir-cR8-BSA-NPs (right) with lysosomes, with LysoTracker in red and Ir-cR8/Ir-cR8-BSA-NPs in green; scale bar, 20 μm. I-J Expression of Ir-cR8 (left) and Ir-cR8-BSA-NP (right) lethal cells; PI is shown in red, and Ir-cR8/Ir-cR8-BSA-NPs are shown in green; scale bar 20 μm. (**K**) Serum stability of Ir-cR8 and Ir-cR8-BSA-NPs; **P<0.01. (**L**) Hemolytic toxicity of Ir-cR8 and Ir-cR8-BSA-NPs; ***P<0.001. (**M**) Cell entry pathway of Ir-cR8-BSA-NPs; It was mainly divided into three major groups: control group, endocytosis pathway inhibition group and energy inhibition group, and each endocytosis inhibition group was added with the caveolin-mediated endocytosis pathway inhibitor Nystatin (NY, working concentration of 9 μg mL^{-1}), the Clathrin-mediated endocytosis pathway inhibitor chlorpromazine (CPZ, working concentration of 2.5 μg mL^{-1}) and the Cytosolic pathway inhibitor cell relaxant (CytoD, the working concentration of 2.5 μg mL^{-1}) The energy inhibition group was incubated at 4°C for 2 hours. **P<0.01.

 https://doi.org/10.2147/IJN.S502257

Table 1 Killing Activity of the NPs Against Three Cell Types

	H22	BMDC	BMDM
IC_{50} (μM)	9.95±0.28	35.16±7.09	40.22±11.37

Cell Entry Pathway of Ir-cR8-BSA-NPs

The mechanisms of membrane-active peptide entry can be grouped into two categories: endocytosis and direct membrane translocation. The endocytosis pathway requires energy and involves mainly caveolin-dependent endocytosis, macropinocytosis and clathrin-dependent endocytosis. To investigate the mechanism of the cellular ingestion of Ir-cR8-BSA-NPs, the decrease in the cellular uptake rate after the addition of each pathway inhibitor and energy inhibition was examined. The results of the study are shown in Figure 2M, where the uptake rate was significantly reduced in the energy inhibition group, suggesting that the cellular entry of Ir-cR8-BSA-NPs is active. There was no significant change in the uptake rate after inhibition of the caveolin-dependent endocytosis pathway compared with the uptake rate of normal entry cells, but the uptake rate of Ir-cR8-BSA-NPs was significantly reduced by inhibition of the macropinocytosis pathway and the clathrin-dependent endocytosis pathway. In summary, the endocytic pathway of Ir-cR8-BSA-NPs is an energy-dependent pathway mediated by macropinocytosis and clathrins.

Intracellular Distribution and Lethal Mechanism of Ir-cR8-BSA-NPs

The intracellular distribution of Ir-cR8 and Ir-cR8-BSA-NPs after they entered the cells was observed by confocal microscopy. The results, as shown in Figure 2G–H, revealed that Ir-cR8 diffused intracellularly, whereas Ir-cR8-BSA-NPs clearly colocalized with lysosomes after entering the cells; the other aspect of the diffusion in the intracellular area was likely the escape of some Ir-cR8 from the lysosomes. There are various types of cell death, and most chemotherapeutic drugs exert their therapeutic effects by killing tumor cells through the induction of apoptosis. Owing to the intrinsic luminescence property of Ir-cR8, the whole process by which Ir-cR8-BSA-NPs interact with cells was observed by confocal microscopy, and the results are shown in Figure 2I–J. The Ir-cR8-BSA-NPs entered the cells to cause cellular swelling, followed by rupture of the cell membrane, entry of propidium iodide (PI) into the cells to stain the nuclei red, and loss of large quantities of cell contents. The whole lethal process of Ir-cR8-BSA-NPs took longer than that of the monomeric peptide Ir-cR8 did, from 39 min to approximately 99 min, probably because the process from cell entry to lysosomal escape to cause cell death following the administration of Ir-cR8-BSA-NPs was more complicated and took longer than that of the peptide alone.

Serum Stability of Ir-cR8-BSA-NPs

Membrane-active peptides are susceptible to hydrolysis by hydrolytic enzymes, and overcoming this drawback is beneficial for the in vivo application of peptides. In Ir-cR8-BSA-NPs, the peptide Ir-cR8 spontaneously forms a highly stable structure with albumin. Because the molecular weight of albumin is approximately 30 times greater than that of Ir-cR8, the spatial site-blocking effect of albumin may hinder the ability of hydrolases to approach Ir-cR8 and protect it from degradation by hydrolases.[34–36] We investigated the loss of cell-killing ability by comparing Ir-cR8 and Ir-cR8-BSA-NPs after incubation with serum. The results, as shown in Figure 2K, revealed that after incubation with serum for 2, 4, 16, and 24 h, the loss of the cell-killing ability of Ir-cR8-BSA-NPs was much lower than that of Ir-cR8, and the loss of the cell-killing ability of Ir-cR8-BSA-NPs after incubation with serum for 24 h was 24.87±4.02%, whereas the loss of the cell-killing ability of Ir-cR8 after incubation with serum for 24 h was 58.42±5.32%, indicating that bovine serum albumin protects the peptide Ir-cR8 against hydrolysis by hydrolases and improves the stability of Ir-cR8 in serum.

Hemolytic Toxicity of Ir-cR8 and Ir-cR8-BSA-NPs

Hemolytic toxicity is one of the major limitations hindering the in vivo application of peptides. The formation of Ir-cR8-BSA-NPs from albumin and Ir-cR8 theoretically prevents Ir-cR8 from directly contacting the erythrocyte membrane to a certain extent, which reduces hemolytic toxicity and improves biosafety. To confirm this, this study incubated Ir-cR8 and Ir-cR8-BSA-NPs with mouse erythrocytes to investigate the hemolytic effects of both. The results, as shown in Figure 2L, revealed that the

https://doi.org/10.2147/IJN.S502257

hemolytic toxicity of Ir-cR8-BSA-NPs was significantly attenuated, with the hemolysis rate of Ir-cR8 close to 100% and that of Ir-cR8-BSA-NPs only 6.37±0.13% at a drug concentration of up to 250 μM, suggesting that albumin was able to significantly ameliorate the hemolytic toxicity and thus improve the safety of the peptide. In vitro experiments have demonstrated the antihepatocellular carcinoma cell potential, killing selectivity, serum stability, and biosafety of peptide drugs, providing a prerequisite and guarantee for the subsequent in vivo application of peptides.

Assessment of Apoptosis and Proliferation by TUNEL and Ki-67 Staining

To further investigate the anti-tumour effects of Ir-cR8-BSA-NPs, we performed TUNEL staining for apoptosis and Ki-67 staining for cell proliferation in H22 mouse hepatocellular carcinoma cell line.We performed TUNEL staining on paraffin-embedded tumour tissue sections from a mouse orthotopic hepatocellular carcinoma model. The results showed a significant increase in the number of TUNEL-positive cells in the Ir-cR8-BSA-NPs-treated group compared to the control group, with an effect similar to that of the oxaliplatin group, suggesting a high level of apoptosis induced by Ir-cR8-BSA-NPs (Supplementary Figure 4A–C).

Ki-67 staining was also performed to assess the proliferation rate of cancer cells. Ki-67-positive cells were significantly reduced in the Ir-cR8-BSA-NPs-treated group compared with the control group, suggesting an inhibitory effect of Ir-cR8-BSA-NPs on cell proliferation (Supplementary Figure 5A–C). A similar effect was observed with Ki-67 staining compared to the oxaliplatin-treated group, which highlights the potential that Ir-cR8-BSA-NPs could be used as an effective anticancer therapy. These staining results provide additional evidence for the anti-tumour efficacy of Ir-cR8-BSA-NPs, demonstrating their ability to induce apoptosis and inhibit cell proliferation in hepatocellular carcinoma models.

In Vivo Experiments

Retention of Ir-cR8-BSA-NPs in Vivo

Peptide drugs face several limitations when administered in vivo, such as a short circulation time due to the presence of various hydrolytic enzymes in the body. The concentration of Ir-cR8-BSA-NPs in the circulation was calculated by taking blood samples at different times after intravenous injection of the drug and measuring the iridium content in the blood. As shown in Supplementary Figure 6, after approximately half an hour, the iridium content of Ir-cR8 in the blood decreased to less than half, whereas the half-life of Ir-cR8-BSA-NPs reached 9.8 hours. This result indicates that the preparation of the peptide as an albumin nanoparticle can significantly prolong the residence time of the peptide drug in the body circulation.

In Vivo Tissue Distribution of Ir-cR8-BSA-NPs

After intravenous injection, the drug enters the bloodstream directly, and as the blood reaches various organs, the drug exerts its effects. In this study, we investigated the distribution of Ir-cR8 and Ir-cR8-BSA-NPs in different organs, especially in tumors, after intravenous injection via the tail vein. As shown in Figure 3D, 24 hours after injection, the levels of Ir-cR8-BSA-NPs in various organs were greater than those of Ir-cR8, possibly due to the increased stability of Ir-cR8-BSA-NPs in the body.

The Ir-cR8-BSA-NPs presented the greatest accumulation in the liver, possibly due to the phagocytic action of the reticuloendothelial system (RES). The RES refers to monocytes produced by the bone marrow with strong phagocytic functions. NPs entering the body are easily engulfed by the RES, and the liver contains numerous fixed reticuloendothelial cells (Kupffer cells), leading to drug accumulation in the liver. In addition, Ir-cR8-BSA-NPs accumulated significantly more in tumor sites than in other organs, as noted by the threefold increase in Ir-cR8 accumulation in tumors; this may be due to the enhanced permeability and retention (EPR) effect, whereby nanoparticles tend to accumulate and remain in tumor tissue owing to the irregular arrangement of blood vessels and the increased vascular permeability in tumors. The abnormal tumor vasculature facilitates the preferential penetration of nanoparticles into the interstitial space, and the lack of lymphatic drainage in tumor tissue slows the movement of nanoparticles in the interstitial space.

Application of a Murine Orthotopic Liver Cancer Model

The establishment of an orthotopic mouse liver cancer model at relevant organ sites provides a better simulation of liver cancer formation and treatment effects. In this study, a mouse orthotopic liver cancer model was used, and the therapeutic efficacy of Ir-cR8-BSA-NPs was investigated using in vivo imaging. Both the Ir-cR8-BSA-NP and oxaliplatin groups effectively inhibited orthotopic tumors in the mice (Figure 3A and B). Notably, some mice in the oxaliplatin group experienced weight loss during

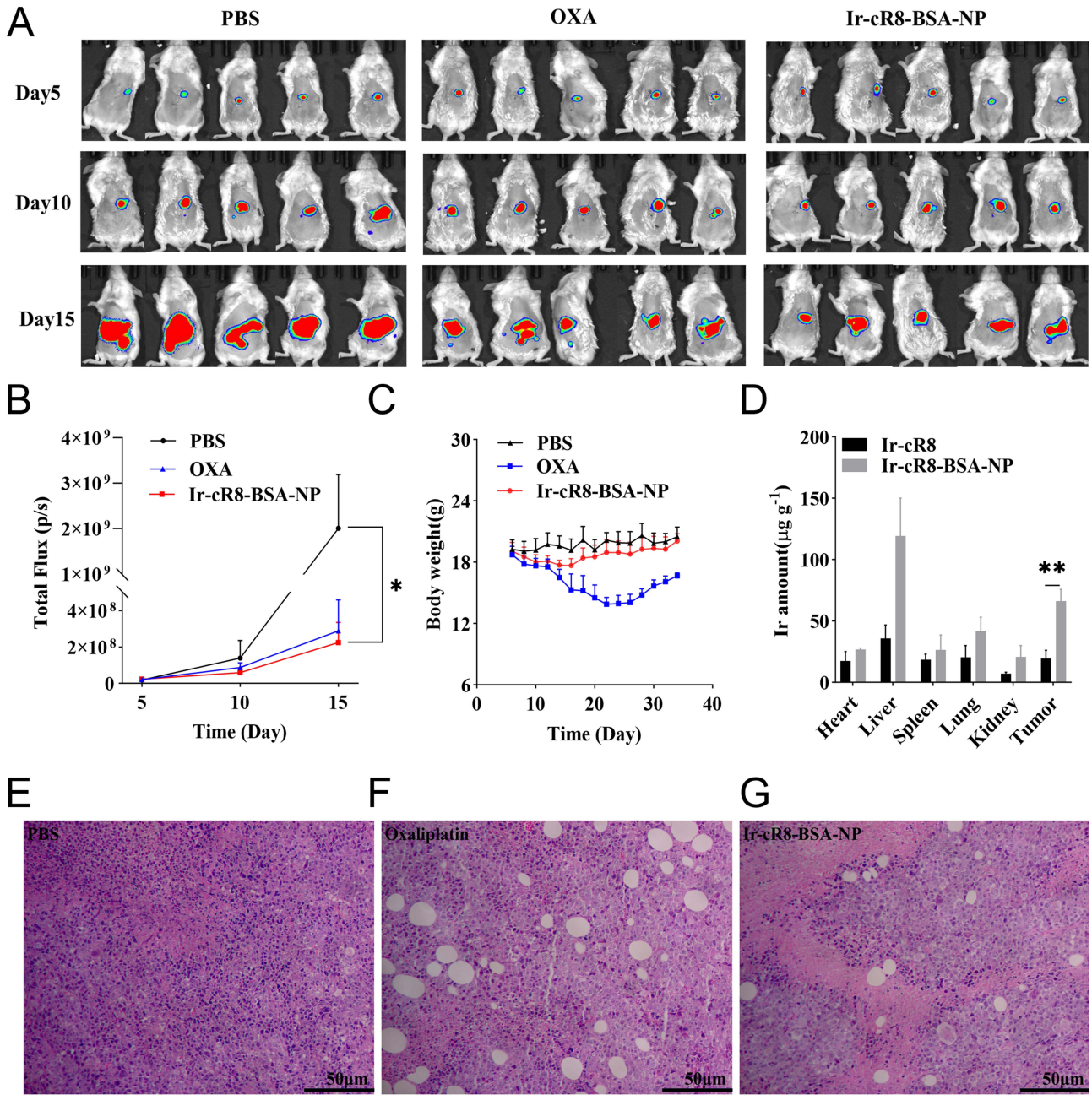

Figure 3 (**A**) In vivo imaging of orthotopic tumors in mice after intravenous injection of Ir-cR8, Ir-cR8-BSA-NPs or oxaliplatin. (**B**) Changes in total fluorescence intensity in in vivo images of orthotopic tumors in mice; *P<0.1. (**C**) Changes in the body weights of the mice in each group after intravenous injection of PBS, Ir-cR8-BSA-NPs or oxaliplatin. (**D**) Tissue distribution of Ir-cR8 and Ir-cR8-BSA-NPs 24 hours after a single intravenous injection; **P<0.01. (**E–G**) Histopathological images of tumors after intravenous injection of PBS; oxaliplatin and Ir-cR8-BSA-NPs were obtained by hematoxylin and eosin (HE) staining.

treatment, with a decrease from the initial 20 g to 13 g (Figure 3C), demonstrating the toxicity of oxaliplatin. In comparison, the intravenous administration of Ir-cR8-BSA-NPs had similar antitumor effects without significant side effects, highlighting the improved safety profile of Ir-cR8-BSA-NPs compared with that of chemotherapeutic drugs. These findings were further confirmed by histological observations of mouse heart, liver, spleen, lung and kidney tissue sections.

After the experiment, the heart, liver, spleen, lung, kidney and tumor tissues of the mice in each group were subjected to HE staining (Supplementary Figure 7) After intravenous administration of various drugs, normal tissues with intact cell morphology and clear contours showed no obvious toxicity. Among the tumor tissues, those in the PBS group were neatly arranged and uniform with clear contours. In contrast, both the oxaliplatin and Ir-cR8-BSA-NPs groups presented reduced numbers of viable cells, incomplete cell structures and noticeable gaps, as shown in Figure 3E–G.

https://doi.org/10.2147/IJN.S502257

Application of the Rabbit VX2 Orthotopic Liver Cancer Model

Interventional therapy has recently emerged as a minimally invasive, efficient, convenient, safe and less complicated treatment modality, resulting in significantly shorter hospital stays.[37–40] In this study, we successfully established a rabbit VXII orthotopic liver tumor model (Figure 4A), and DSA-guided Ir-cR8-BSA NPs were administered via hepatic artery perfusion, as shown in Figure 4B. In contrast to conventional intravenous chemotherapeutic drugs, this approach allows

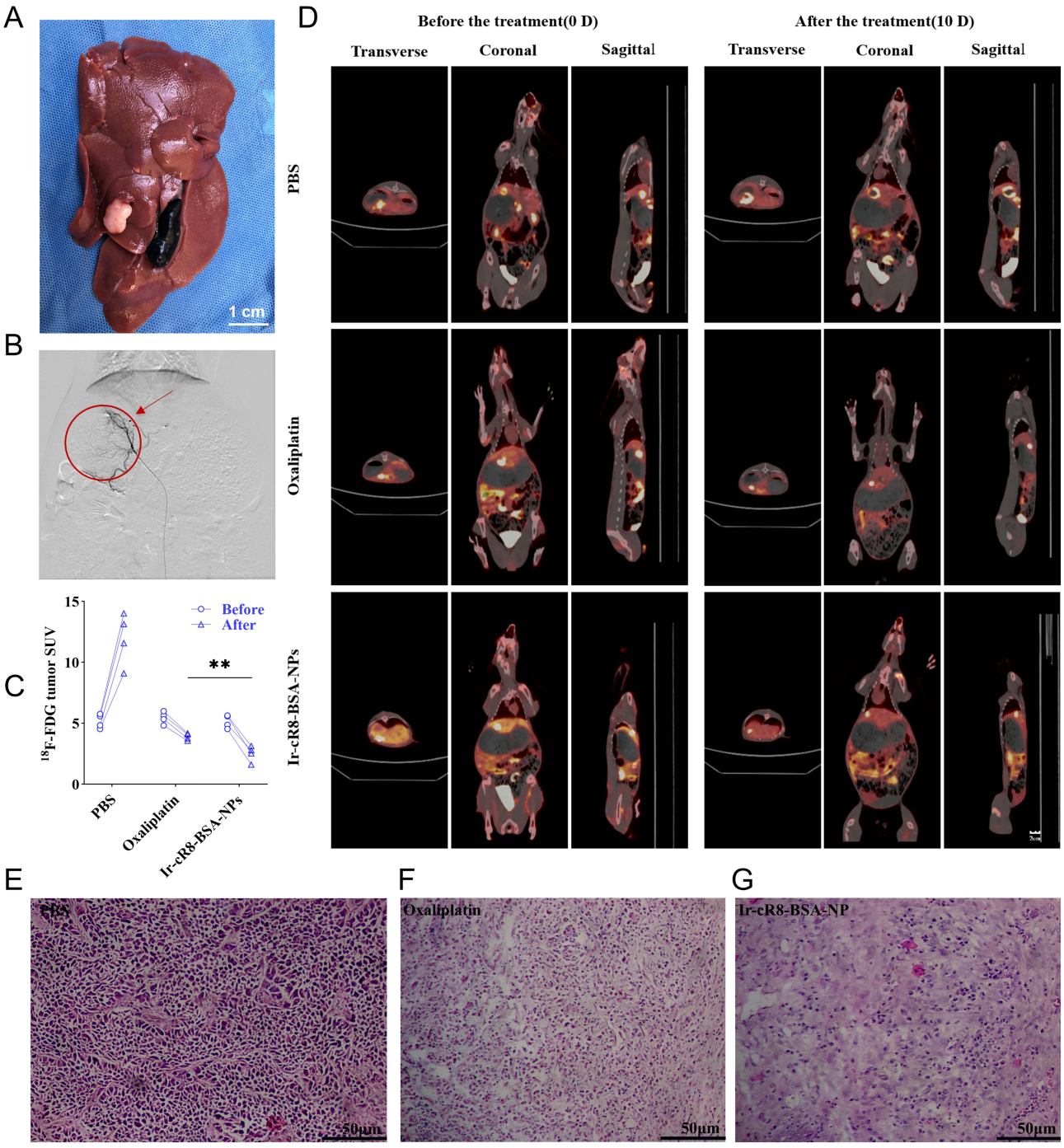

Figure 4 (**A**) Solid study of liver and liver tumors in rabbits, scale bar is 1 cm. (**B**) Experimental imaging of liver tumor contrast silhouettes under DSA in rabbits. The Arrow and circle indicate the contrasted liver tumors. (**C**) Changes in standardized uptake value (SUV) before and after treatment of orthotopic tumors in rabbits; **P<0.01. (**D**) PET/CT imaging results of rabbits before and after orthotopic liver tumor development. (**E–G**) Histopathological images of rabbit liver tumors after arterial infusion of PBS, oxaliplatin, and Ir-cR8-BSA-NPs treatment with hematoxylin and eosin (HE) staining.

direct action at the lesion site, significantly increasing the drug concentration at the lesion site while reducing systemic drug toxicity. Following arterial infusion treatment, therapeutic efficacy was assessed using PET/CT imaging in the tumor-bearing rabbits in each group. As shown in Figure 4C and D, the tumor standardized uptake value (SUV) in the Ir-cR8-BSA-NPs group decreased from 5.15±0.46 to 2.52±0.57, whereas that in the oxaliplatin group decreased from 5.44 ±0.43 to 3.90±0.24. These results indicate a statistically significant benefit of Ir-cR8-BSA-NPs treatment over oxaliplatin. The tumor tissues in the rabbits were examined after therapy. Tumor histology by HE staining, as shown in Figure 4E–G, indicated that the PBS group had dense and uniform tumor cells with clear cell contours; the oxaliplatin group presented some tumor cells without intact cell structures and with large gaps; and the Ir-cR8-BSA-NPs group presented severe tissue damage, disordered cell arrangement and distorted cell contours. The differences in tissue structure between the groups were consistent with the changes in the SUV values determined by tumor imaging. Compared with oxaliplatin, Ir-cR8-BSA-NPs therefore demonstrated superior tumor suppression properties, highlighting their potential as an effective treatment for orthotopic liver tumors.

Conclusion

This study represents an important advance in the field of hepatocellular carcinoma (HCC) research, addressing the urgent need for more effective and less toxic HCC treatment options. We successfully demonstrated the potential of a novel nanomedicine, Ir-cR8-BSA-NPs, which combines the anticancer properties of iridium-coordinated octaarginine peptide (Ir-cR8) with the stabilization and targeting advantages of albumin. This innovative approach not only enhances the stability and bioavailability of the peptide, but also reduces its hemolytic toxicity, making it a promising candidate for interventional treatment of hepatocellular carcinoma. Our findings suggest that Ir-cR8-BSA-NPs show superior anti-tumor effects over oxaliplatin, both in vitro and in vivo. This nanoparticle showed potent inhibition of tumor growth, reduced systemic toxicity and improved therapeutic efficacy in an in situ hepatocellular carcinoma model. In particular, in Supplementary Figure 8, we demonstrate the successful isolation of the femoral artery (A) and introduction of a microcatheter (B) via arterial puncture, which further demonstrates the potential application of Ir-cR8-BSA-NPs in interventional therapy. This study highlights the advantages of the combination of a novel membrane-active tumor-lysing peptide nanomedicine and precise drug delivery enabled by arterial perfusion technology for interventional therapy of hepatocellular carcinoma. Looking forward, the future direction of this nanomedicine lies in its potential for translation to the clinic. In addition, exploring the synergistic effects of Ir-cR8-BSA-NPs with other therapeutic modalities, such as immunotherapies, may open new avenues for combination therapies that offer greater benefits. The development of Ir-cR8-BSA-NPs represents an important step towards more effective and less toxic liver cancer treatment options, offering hope for improved prognosis and quality of life for patients.

Consent for Publication

All the authors agree to publish.

Acknowledgments

This paper has been uploaded to ResearchSquare as a preprint: https://www.researchsquare.com/article/rs-4374218/v1

Funding

This work was funded by the Medical Research Project of Jiangsu Provincial Health Commission (ZD2022024), the Research Project of China Baoyuan Investment Co., Ltd., and the Suzhou Science and Technology Plan Project (SKY2023051), The Ministry of Science and Technology of Jiangsu Province (Key Research and Development Project BE2021666).

Disclosure

The authors declare that they have no competing interests.

References

1. Singal A, Kanwal F, Llovet J. Global trends in hepatocellular carcinoma epidemiology: implications for screening, prevention and therapy. *Nat Rev Clin Oncol*. 2023;20:864–884. doi:10.1038/s41571-023-00825-3
2. Llovet J, Castet F, Heikenwalder M, et al. Immunotherapies for hepatocellular carcinoma. *Nat Rev Clin Oncol*. 2022;19:151–172. doi:10.1038/s41571-021-00573-2
3. Sung H, Ferlay J, Siegel RL, et al. Global cancer statistics 2020: GLOBOCAN estimates of incidence and mortality worldwide for 36 Cancers in 185 Countries. *CA Cancer J Clin*. 2021;71:209–249. doi:10.3322/caac.21660
4. Llovet J, Kelley R, Villanueva A, et al. Hepatocellular carcinoma. *Nature Reviews. Disease Primers*. 2021;7:6. doi:10.1038/s41572-020-00240-3
5. Yip T, Lee H, Chan W, Wong G, Wong V. Asian perspective on NAFLD-associated HCC. *Journal of Hepatology*. 2022;76:726–734. doi:10.1016/j.jhep.2021.09.024
6. Foerster F, Gairing S, Müller L, Galle P. NAFLD-driven HCC: safety and efficacy of current and emerging treatment options. *Journal of Hepatology*. 2022;76:446–457. doi:10.1016/j.jhep.2021.09.007
7. Saito Y, Yin D, Kubota N, et al. A therapeutically targetable TAZ-TEAD2 pathway drives the growth of hepatocellular carcinoma via ANLN and KIF23. *Gastroenterology*. 2023;164:1279–1292. doi:10.1053/j.gastro.2023.02.043
8. Reig M, Forner A, Rimola J, et al. BCLC strategy for prognosis prediction and treatment recommendation: the 2022 update. *Journal of Hepatology*. 2022;76:681–693. doi:10.1016/j.jhep.2021.11.018
9. Ning L, Youen L, Yanan K, et al. FOXAI: a Phase II trial evaluating the efficacy and safety of hepatic arterial infusion of oxaliplatin plus fluorouracil/leucovorin for advanced hepatocellular carcinoma. *Gut*. 2018;67(2):395–396. doi:10.1136/gutjnl-2017-314138
10. Tian-Qi Z, Zhi-Jun G, Meng-Xuan Z, et al. Camrelizumab (a PD-1 inhibitor) plus apatinib (an VEGFR-2 inhibitor) and hepatic artery infusion chemotherapy for hepatocellular carcinoma in Barcelona Clinic Liver Cancer Stage C (TRIPLET): a phase II study. *Signal Transduct Target Ther*. 2023;8(1):413. doi:10.1038/s41392-023-01663-6
11. Kim S, Lee H, Hong J, et al. Bone-targeted delivery of cell-penetrating-RUNX2 fusion protein in osteoporosis model. advanced science (Weinheim, Baden-Wurttemberg. *Germany*. 2023;10:e2301570. doi:10.1002/advs.202301570
12. Vedadghavami A, Zhang C, Bajpayee A. Overcoming negatively charged tissue barriers: drug delivery using cationic peptides and proteins. *Nano Today*. 2020;34:100898. doi:10.1016/j.nantod.2020.100898
13. Ji S, Huang L, Chang S, et al. Albumin pre-opsonized membrane-active iPep nanomedicine potentiates chemo to immunotherapy of cancer. *Biomaterials*. 2023;301:122269. doi:10.1016/j.biomaterials.2023.122269
14. Lin W, Liu Y, Wang J, et al. Engineered bacteria labeled with iridium(iii) photosensitizers for enhanced photodynamic immunotherapy of solid tumors. angewandte chemie (International ed. in English). *Angewandte Chemie*. 2023;62:e202310158. doi:10.1002/anie.202310158
15. Tong K, Wu C, Wu Y, et al. Cascading energy transfer for highly efficient deep-red OLED Emission with Cyclometalated [3+2+1] iridium complexes. *Small*. 2023;20:e2307500. doi:10.1002/smll.202307500
16. Zhang D, Zheng Y, Zhang H, et al. Delivery of phosphorescent anticancer iridium(III) complexes by polydopamine nanoparticles for targeted combined photothermal-chemotherapy and thermal/photoacoustic/lifetime imaging. *Advanced Science*. 2018;5:1800581. doi:10.1002/advs.201800581
17. Ji S, Yang X, Chen X, et al. Structure-tuned membrane active Ir-complexed oligoarginine overcomes cancer cell drug resistance and triggers immune responses in mice. *Chemical Science*. 2020;11:9126–9133. doi:10.1039/d0sc03975f
18. Caraceni P, O'Brien A, Gines P. Long-term albumin treatment in patients with cirrhosis and ascites. *Journal of Hepatology*. 2022;76:1306–1317. doi:10.1016/j.jhep.2022.03.005
19. Wong J, Ekanayake A, Kharchenko S, et al. Genetically encoded discovery of perfluoroaryl macrocycles that bind to albumin and exhibit extended circulation in vivo. *Nat Commun*. 2023;14:5654. doi:10.1038/s41467-023-41427-y
20. Yasuda K, Maeda H, Kinoshita R, et al. Encapsulation of an antioxidant in redox-sensitive self-assembled albumin nanoparticles for the treatment of hepatitis. *ACS nano*. 2023;17:16668–16681. doi:10.1021/acsnano.3c02877
21. Qin Y, Sun R, Gianoulis N, Nocera D. Photoredox Nickel-Catalyzed C-S Cross-Coupling: mechanism, Kinetics, and Generalization. *J Am Chem Soc*. 2021;143:2005–2015. doi:10.1021/jacs.0c11937
22. Tanaka N, Zhu J, Valencia O, Schull C, Scheidt K. Cooperative carbene photocatalysis for β-amino ester synthesis. *J Am Chem Soc*. 2023. doi:10.1021/jacs.3c09875
23. Tian J, Liu J, Hu Z, Chen X. Interaction of wogonin with bovine serum albumin. *Bioorganic & Medicinal Chemistry*. 2005;13:4124–4129. doi:10.1016/j.bmc.2005.02.065
24. Ni Y, Wang S, Kokot S. Spectrometric study of the interaction between alpinetin and bovine serum albumin using chemometrics approaches. *Analytica chimica acta*. 2010;663:139–146. doi:10.1016/j.aca.2010.01.053
25. Ngambenjawong C, Chan L, Fleming H, Bhatia S. Conditional antimicrobial peptide therapeutics. *ACS nano*. 2022;16:15779–15791. doi:10.1021/acsnano.2c04162
26. Liu Y, Bai X, Lyu C, et al. Mechano-bioconjugation strategy empowering fusion protein therapeutics with aggregation resistance, prolonged circulation, and enhanced antitumor efficacy. *J Am Chem Soc*. 2022;144:18387–18396. doi:10.1021/jacs.2c06532
27. Guo J, Sun J, Liu X, Wang Z, Gao W. Head-to-tail macrocyclization of albumin-binding domain fused interferon alpha improves the stability, activity, tumor penetration, and pharmacology. *Biomaterials*. 2020;250:120073. doi:10.1016/j.biomaterials.2020.120073
28. Zhu Y, Xia T, Chen D, et al. Promising role of protein arginine methyltransferases in overcoming anti-cancer drug resistance. Drug resistance updates: reviews and commentaries in antimicrobial and anticancer chemotherapy. *Drug Resistance Updates*. 2023;72:101016. doi:10.1016/j.drup.2023.101016
29. Vieito M, Moreno V, Spreafico A, et al. Phase 1 study of JNJ-64619178, a protein arginine methyltransferase 5 inhibitor, in advanced solid tumors. *Clinical Cancer Research: an Official Journal of the American Association for Cancer Research*. 2023;29:3592–3602. doi:10.1158/1078-0432.Ccr-23-0092
30. Liu J, Bu X, Chu C, et al. (2023) PRMT1 mediated methylation of cGAS suppresses anti-tumor immunity. *Nat Commun*. 2023;14:2806. doi:10.1038/s41467-023-38443-3
31. Shi Y, Niu Y, Yuan Y, et al. (2023) PRMT3-mediated arginine methylation of IGF2BP1 promotes oxaliplatin resistance in liver cancer. *Nat Commun*. 1932;14. doi:10.1038/s41467-023-37542-5

32. Kureshi R, Bello E, Kureshi C, et al. DGKα/ζ inhibition lowers the TCR affinity threshold and potentiates antitumor immunity. *Science Advances*. 2023;9:eadk1853. doi:10.1126/sciadv.adk1853
33. Lu T, Hu X, van Haren M, Spruijt E, Huck W. Structure-property relationships governing membrane-penetrating behaviour of complex coacervates. *Small*. 2023;19:e2303138. doi:10.1002/smll.202303138
34. Li S, Wang Y, Wang X, et al. Macrocyclic-albumin conjugates for precise delivery of radionuclides and anticancer drugs to tumors. *ACS nano*. 2023;17:22399–22409. doi:10.1021/acsnano.3c04718
35. Shi Z, Luo M, Huang Q, et al. NIR-dye bridged human serum albumin reassemblies for effective photothermal therapy of tumor. *Nat Commun*. 2023;14:6567. doi:10.1038/s41467-023-42399-9
36. Yang Y, Li X, Song J, et al. Structure-activity relationship of pH-sensitive doxorubicin-fatty acid prodrug albumin nanoparticles. *Nano Letters*. 2023;23:1530–1538. doi:10.1021/acs.nanolett.2c04976
37. Zhu H, Li H, Huang M, et al. Transarterial chemoembolization with PD-(L)1 inhibitors plus molecular targeted therapies for hepatocellular carcinoma (CHANCE001). *Signal Transduction and Targeted Therapy*. 2023;8:58. doi:10.1038/s41392-022-01235-0
38. Chen M, Shu G, Lv X, et al. HIF-2α-targeted interventional chemoembolization multifunctional microspheres for effective elimination of hepatocellular carcinoma. *Biomaterials*. 2022;284:121512. doi:10.1016/j.biomaterials.2022.121512
39. Kawaguchi Y, Hasegawa K, Hagiwara Y, et al. Effect of diameter and number of hepatocellular carcinomas on survival after resection, transarterial chemoembolization, and ablation. *The American Journal of Gastroenterology*. 2021;116:1698–1708. doi:10.14309/ajg.0000000000001256
40. Shin S, Ahn K, Kim S, Kim T, Kim Y, Kang K. Liver resection versus local ablation therapies for hepatocellular carcinoma within the Milan criteria: a systematic review and meta-analysis. *Ann Surg*. 2021;273:656–666. doi:10.1097/sla.0000000000004350